

## Inner-shell resonant absorption effects on evolution dynamics of the charge state distribution in a neon atom interacting with ultraintense x-ray pulses

Wenjun Xiang, Cheng Gao, Yongsheng Fu, Jiaolong Zeng,\* and Jianmin Yuan

*Department of Physics, College of Science, National University of Defense Technology, Changsha Hunan, People's Republic of China, 410073*

(Received 7 September 2012; published 11 December 2012)

Inner-shell resonant absorption (IRA) effects were investigated on evolution dynamics of charge state distribution (CSD) in the interaction of ultraintense x-ray pulses with a neon atom. IRA is the physical origin of the large discrepancies found between theory and experiment at a photon energy of 1050 eV [L. Young *et al.*, *Nature (London)* **466**, 56 (2010)], where the rates of  $K$ -shell resonant absorption  $1s \rightarrow 4p$  of  $\text{Ne}^{6+}$  and  $1s \rightarrow 3p$  of  $\text{Ne}^{7+}$  are larger than the direct single-photon ionization rates by more than one order of magnitude, and hence IRA becomes the dominant absorption mechanism. Only when the IRA effects are properly taken into account can we correctly explain the observed CSD.

DOI: [10.1103/PhysRevA.86.061401](https://doi.org/10.1103/PhysRevA.86.061401)

PACS number(s): 32.80.Wr, 52.20.-j, 52.25.Jm, 52.38.-r

Strong-field physics, an extreme limit of light-matter interaction, is expanding from the long-wavelength regime into the short-wavelength region due to technological advancements in x-ray free-electron lasers such as the Linac Coherent Light Source (LCLS) [1]. Understanding the x-ray absorption mechanisms at a fundamental level is the basis of any further investigations and is essential for all types of applications. The first experiment at the LCLS carried out by Young *et al.* [2] revealed that a sequential  $K$ -shell single-photon ionization mechanism dominates the interaction in the electronic response of a free neon atom to a single  $\sim 100$  fs (femtosecond) x-ray pulse at ultrahigh intensity up to  $10^{18}$  W cm $^{-2}$ . This experiment opened a new era of exploring the interaction of high-intensity x rays with matter and opened the way to a theoretical understanding of photoabsorption mechanisms accessed by the LCLS. Then a series of important experiments [3–7] corroborated the sequential multiple photoionization mechanism, with direct nonlinear two-photon ionization playing a role in the interaction [5,8,9]. These pioneer experiments investigated photoabsorption mechanisms by measuring the charge state distributions (CSDs), which is of fundamental importance for any further studies such as the equation of state and radiative property in astrophysics [10], warm dense matter [11], and inertial confinement fusion research [12].

In order to understand the photoabsorption mechanism in matter interactions with ultraintense x-ray pulses, a time-dependent rate equation (TDRE) approach [8] was employed to calculate the CSD. It was found that there were good agreements at photon energies of 800 and 2000 eV, which are far removed from resonances, while discrepancies were evident where resonances exist (at 1050 eV) [2]. The discrepancies imply that our understanding of the photoabsorption mechanism is incomplete. To the best of our knowledge, the effects of the inner-shell resonant absorption (IRA) have never been investigated before in interactions with high-intensity x rays. In this Rapid Communication we show that IRA is the main reason for such discrepancies between theory and experiment.

Resonant photopumping of  $K$ -shell electrons to the  $L$ ,  $M$ , or even higher bound orbitals (rather than to the continuum) is not in itself novel, being a typical physical picture of the photoionization process: a smooth background (direct photoionization) superimposed by a series of resonances. Resonances provide an interaction strength that is two or three orders of magnitude larger than that in the continuum. However, the IRA mechanism was not discussed in the pioneer experiments [2–7]. These experiments utilized intense, quasi-monochromatic x-ray photons in so narrow a photon energy range that the authors might have omitted the contributions of the  $K$ -shell resonances in the photoionization cross section. Young *et al.* [2] estimated a bandwidth of 0.5%, which is indeed very narrow (about 5 eV at 1050 eV). Within this narrow bandwidth, the intensity of an x-ray pulse varies rapidly from nearly zero to  $10^{18}$  W cm $^{-2}$  over an ultrashort pulse duration of  $\sim 100$  fs. To properly account for the IRA effects, one has to obtain a complete set of accurate atomic data including resonance position and line strength, which is difficult to achieve for a statistical method that includes items such as an unresolved transition array [13], supertransition [14], and an average atom [15], and thus poses challenges in modeling.

To investigate the IRA effects, we developed a detailed level accounting (DLA) method on the relevant atoms in the TDRE formalism. The DLA scheme has been widely used in the calculations of the radiative property of hot dense plasmas in local thermodynamic equilibrium (LTE) [16,17] and has successfully resolved the longstanding discrepancies between theory and experiment for high- $Z$  plasmas [18]. However, such a DLA method has not been applied in studies of x-ray-matter interactions, where the ionization balance is determined by all microscopic processes due to photons and electrons [19,20]. The population distribution is determined by a set of coupled TDREs,

$$\frac{dN_i}{dt} = \sum_i N_i R_{ij} - \sum_j N_j R_{ji}, \quad (1)$$

where  $N_i$  is the population of level  $i$ , and  $R_{ji}$  and  $R_{ij}$  are the populating and depopulating rates due to different atomic processes, including photoexcitation and ionization, electron impact excitation and ionization, Auger decay (AD), and their reverse processes. Two-electron processes such as direct

\*Author to whom correspondence should be addressed: [jlzeng@nudt.edu.cn](mailto:jlzeng@nudt.edu.cn)

double Auger [21,22] and double photoionization (PI) [23,24] were also included in the rate equation. The rate coefficients were calculated from cross sections of the above-mentioned microscopic processes [25,26]. The required cross sections for single-photon and single-electron processes are calculated by a fully relativistic approach based on the Dirac equation [27,28] in a fine-structure level formalism. Atomic data for direct two-electron processes were obtained by our developed code with the wave function derived in Refs. [27,28]. To take the resonant absorptions into account, the maximum principal quantum number is taken to be 10 in our atomic model. Spatial and temporal averaging was done to obtain the CSD over the interaction volume and pulse duration, assuming an elliptical Gaussian beam profile. The measured pulse shape, if obtainable, can be used to take into account the effect of noisy and spiky pulses at LCLS on laser-driven processes (PI and AD). Yet the measurement is usually difficult.

In the TDRE approach, the populating and depopulating rates determine the level population distributions. In what follows, we first analyze the relevant atomic processes that occurred in the interaction of x-ray pulses with neon. The ionization potential (IP) of a  $1s$  electron in neutral neon is 870 eV. At a photon energy of 800 eV, only valence shell electrons  $2s$  and  $2p$  can be photoionized. Around this photon energy, there is IRA from the levels of  $1s^2 2p^6 3l$  ( $l = s, p, d$ ) ( $\text{Ne}^+$ ) and from  $1s^2 2s^2 2p^3 3p$  and  $1s^2 2s^2 2p^3 4p$  ( $\text{Ne}^{2+}$ ). Yet the populations of these levels are negligible and as a result they have trivial effects on the CSD. At 2000 eV, the transition energy from all relevant ionization stages is far away from it and thus there is no pathway for IRA. At 1050 eV, however, the IRA plays pivotal roles, as can be seen from the following analysis. To better understand this physical mechanism, we list in Table I the  $1s$  IP and ionization cross section of  $\text{Ne}^{4+}$ - $\text{Ne}^{6+}$ , whose  $1s$  IP is around 1050 eV. There are no direct  $1s$  PI channels for charge states higher than  $\text{Ne}^{5+}$ , whose  $1s$  IP (1045.6 eV) is a little smaller than 1050 eV. Such a fact implies that there can be many inner-shell resonant transitions around a photon energy of 1050 eV. As illustrative examples, Table II shows a few strong core-excited transitions for  $\text{Ne}^{3+}$ - $\text{Ne}^{7+}$ . For  $\text{Ne}^{3+}$ ,  $1s \rightarrow 4p$  resonances from levels of single-core configurations of  $1s 2l^6$  (i.e.,  $1s 2s^2 2p^4$ ,  $1s 2s 2p^5$ , and  $1s 2p^6$ ) are located near 1050 eV. These single-core levels can be effectively populated by  $1s$  ionization from  $\text{Ne}^{2+}$ . There are 148 spectral lines in total for such transitions with a weighted oscillator strength  $gf$  greater than  $1.0 \times 10^{-4}$  within 5 eV of 1050 eV. The  $1s \rightarrow 3p$  resonances from levels of  $1s 2l^5$  ( $l = s, p$ ) of  $\text{Ne}^{4+}$  also fall into this type, with 170 lines in total. The resonant absorption from these two charge states of  $\text{Ne}^{3+}$  and  $\text{Ne}^{4+}$  can produce hollow atoms, which is the

TABLE I. The  $1s$  ionization potential (IP) (eV) and ionization cross section (ICS) (Mb) for the ground level of charge states (CS)  $\text{Ne}^{4+}$ - $\text{Ne}^{7+}$ .

CS	Ground config.	$1s$ IP	$1s$ ICS
$\text{Ne}^{4+}$	$1s^2 2s^2 2p^2$	998.6	0.138
$\text{Ne}^{5+}$	$1s^2 2s^2 2p$	1045.6	0.111
$\text{Ne}^{6+}$	$1s^2 2s^2$	1097.3	
$\text{Ne}^{7+}$	$1s^2 2s$	1143.1	

TABLE II. Resonance type (RT), position (RP) (eV), and weighted oscillator strengths ( $gf$ ) for representative core-excited transitions near the photon energy of 1050 eV for  $\text{Ne}^{3+}$ - $\text{Ne}^{7+}$ .

CS	RT	RP	$gf$
$\text{Ne}^{3+}$	$1s 2s^2 2p^4 - 2s^2 2p^4 4p$	1050.75	0.025
$\text{Ne}^{4+}$	$1s 2s^2 2p^3 - 2s^2 2p^3 3p$	1052.36	0.074
$\text{Ne}^{4+}$	$1s 2s 2p^4 - 2s 2p^4 3p$	1051.93	0.063
$\text{Ne}^{4+}$	$1s 2p^5 - 2p^5 3p$	1049.15	0.027
$\text{Ne}^{5+}$	$1s^2 2p^3 - 1s 2p^3 9p$	1046.53	0.0010
$\text{Ne}^{5+}$	$1s 2p^4 - 2s 2p^3 3d$	1051.42	0.0023
$\text{Ne}^{6+}$	$1s^2 2s^2 - 1s 2s^2 4p$	1053.51	0.038
$\text{Ne}^{6+}$	$1s^2 2s 2p - 1s 2s 2p 4p$	1047.76	0.068
$\text{Ne}^{6+}$	$1s^2 2p^2 - 1s 2p^2 4p$	1046.55	0.046
$\text{Ne}^{7+}$	$1s^2 2s - 1s 2s 3p$	1048.92	0.041
$\text{Ne}^{7+}$	$1s^2 2s - 1s 2s 3p$	1048.97	0.080

physical origin of x-ray transparency. With the increase of ionization stages, the inner-shell transitions originate from levels of ground, first, and second excited configurations: the  $1s - np$  ( $n > 6$ ) resonances from  $1s^2 2l^3$  of  $\text{Ne}^{5+}$ ,  $1s \rightarrow 4p$  from  $1s^2 2l^2$  of  $\text{Ne}^{6+}$ , and  $1s \rightarrow 3p$  from  $1s^2 2l$  of  $\text{Ne}^{7+}$ . Some of these core-excited spectral lines have been identified in previous experiments [29,30]. The initial levels of these resonances can be effectively photopumped and therefore they are vital to determine the evolution dynamics of CSD.

The opening of resonant absorption channels presented above will certainly modify the physical picture of x-ray-laser-atom interactions. To have a quantitative understanding of the IRA effects, we give the PI rates and AD rates in Fig. 1(a) and the resonant absorption and corresponding AD rates in Fig. 1(b). As there are many decay channels, the data given in Fig. 1 refer to the rate from the ground level for PI and resonant excitation and to the decay rate of the lowest level with one  $1s$  hole configuration due to  $1s$  ionization or resonant excitation for AD. For example,  $\text{Ne}^{4+}$  AD refers to the decay rate from the lowest levels belonging to configurations of  $1s 2s^2 2p^3$  and  $1s 2s^2 2p^2 3p$ , respectively, in Figs. 1(a) and 1(b). The PI and IRA rates were obtained from intensity  $I(h\nu)$  and cross section  $\sigma_{ij}(h\nu)$  of the corresponding microscopic processes [25],

$$R_{ij} = \int_{\text{IP}}^{\infty} \frac{I(h\nu)}{h\nu} \sigma_{ij}(h\nu) d(h\nu), \quad (2)$$

where  $h\nu$  is the photon energy and IP is the ionization or excitation potential. The dependence of  $I(h\nu)$  on time and space is not explicitly shown for simplicity. A pulse duration of 120 fs was assumed by test calculations with a best fit to the experiment. The PI rate at the peak intensity for  $\text{Ne}^{4+}$  and  $\text{Ne}^{5+}$  is on the order of magnitude of  $1.0 \times 10^{14} \text{ s}^{-1}$ , while that of  $\text{Ne}^{6+}$  and  $\text{Ne}^{7+}$  is nearly an order of magnitude smaller. Such a fact is evident as the PI rate of the latter two charge states originates from the ionization of the valence electron, which is much smaller than that of the  $1s$  electron. The corresponding AD rate after  $1s$  PI is  $1.0 \times 10^{14} \text{ s}^{-1}$ , which is a little smaller than the peak PI rates of  $\text{Ne}^{4+}$  and  $\text{Ne}^{5+}$ . In contrast, the IRA rates shown in Fig. 1(b) can be much larger than the  $1s$  PI rates. The peak IRA rates due to  $1s \rightarrow 3p$  of  $\text{Ne}^{7+}$  and  $1s \rightarrow 4p$  of  $\text{Ne}^{6+}$  are, respectively, about one and four times larger than the  $1s$  PI rates. Such a conclusion means that, for  $\text{Ne}^{6+}$

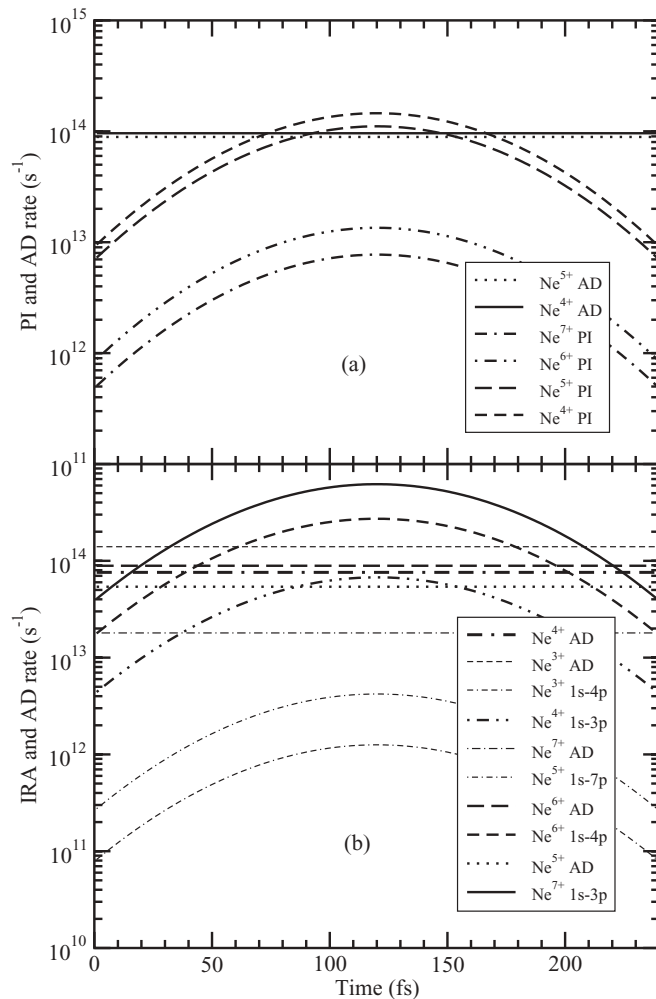


FIG. 1. Rates for (a) PI and followed AD, and (b) inner-shell resonant absorption and followed AD at a photon energy of 1050 eV. The calculation is conducted with a Gaussian beam (120 fs full width at half maximum) centered at 120 fs.

and  $\text{Ne}^{7+}$ , the IRA is the dominant absorption mechanism in determining the evolution dynamics of the system. The atomic processes shown in Fig. 1(a) were considered in Ref. [2], yet those in Fig. 1(b) have not been investigated in ultraintense x-ray-laser-matter interactions. Considering the predominance of IRA and the vast number of resonant lines, one can imagine that the inclusion of IRA effects will admittedly change the physical picture of photoabsorption.

Utilizing the IRA mechanism revealed in Fig. 1(b), we can first qualitatively understand the discrepancies of CSD for  $\text{Ne}^{6+}$ ,  $\text{Ne}^{7+}$ , and  $\text{Ne}^{8+}$  between theory and experiment. The theory overestimated the population of  $\text{Ne}^{6+}$  by a factor of 3, yet underestimated that of  $\text{Ne}^{8+}$  by about the same factor. The reason for the discrepancies is due to the neglect of the IRA mechanism of  $1s \rightarrow 4p$  ( $\text{Ne}^{6+}$ ) and  $1s \rightarrow 3p$  ( $\text{Ne}^{7+}$ ). As the  $1s$  ionization channels are closed for  $\text{Ne}^{6+}$ , only valence ionization contributes to the PI rate, which is small ( $1.0 \times 10^{13} \text{ s}^{-1}$  at peak intensity) compared with that of the  $1s \rightarrow 4p$  resonance absorption ( $2.0 \times 10^{14} \text{ s}^{-1}$  at peak intensity). As a result, the population of  $\text{Ne}^{6+}$  does not have effective depopulating channels and thus their theory overestimates its

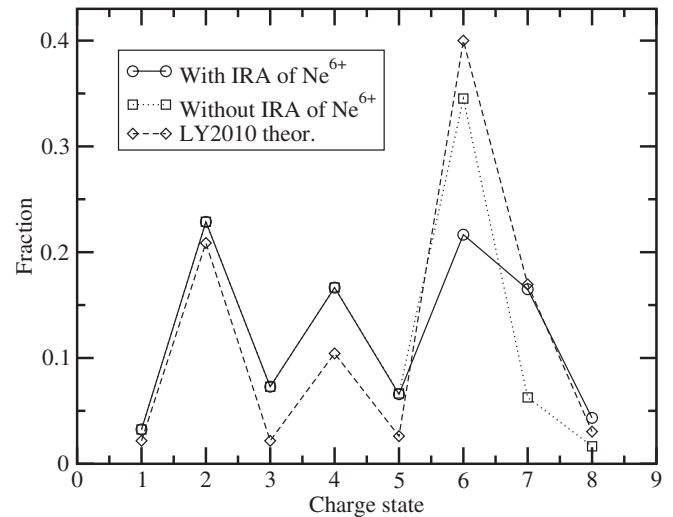


FIG. 2. Effects of IRA  $1s \rightarrow 4p$  of  $\text{Ne}^{6+}$  on CSD produced by 1050-eV photon beams. Circles: With ionization mechanisms given in Fig. 1(a) and inner-shell resonance  $1s \rightarrow 4p$  of  $\text{Ne}^{6+}$ . Squares: With ionization mechanism shown in Fig. 1(a). Diamonds: Theoretical result obtained by Young *et al.* [2].

fraction. With the inclusion of  $1s \rightarrow 4p$  absorption, the ions are photopumped to levels of  $1s2l^24p$  configurations. These levels are autoionized ones and have a large Auger decay rate ( $1.0 \times 10^{14} \text{ s}^{-1}$ ) to the higher ionization stage  $\text{Ne}^{7+}$ . In such a way, the population of  $\text{Ne}^{6+}$  will be dramatically populated to  $\text{Ne}^{7+}$ .

In what follows, we quantitatively demonstrate the IRA effects on the evolution of CSD by two sets of calculations, with one only including atomic processes given in Fig. 1(a) and the other including those in Fig. 1(a) and IRA from  $1s \rightarrow 4p$  of  $\text{Ne}^{6+}$ . Figure 2 shows the CSD with circles and squares, respectively, referring to the results with and without this IRA channel. Without this channel, our theory predicts a fraction of 34% for  $\text{Ne}^{6+}$  and 6% for  $\text{Ne}^{7+}$ . With the opening of this channel, however, the population fraction is 21% and 16%, respectively, for  $\text{Ne}^{6+}$  and  $\text{Ne}^{7+}$ , which is in much better agreement with the experiment. This definitely demonstrated that the  $1s \rightarrow 4p$  absorption of  $\text{Ne}^{6+}$  is the main physical origin of the discrepancy of the  $\text{Ne}^{6+}$  population between experiment and theory (diamonds) [2], which predicted an even higher fraction of  $\text{Ne}^{6+}$  (40%).

A similar argument applies to the population of  $\text{Ne}^{7+}$  and  $\text{Ne}^{8+}$ . With the inclusion of an effective  $1s \rightarrow 3p$  resonance pump of  $\text{Ne}^{7+}$ , the fraction of  $\text{Ne}^{8+}$  is evidently increased. Yet the theoretical result is still lower than the experimental result; this is because there are other resonant channels which affect the evolution dynamics of CSD. From Table II, we know that the  $1s \rightarrow 3p$  resonances of  $\text{Ne}^{7+}$  can only pump populations from levels of  $1s^22l$ . As pointed out above, the strong resonant channel of  $1s \rightarrow 4p$  in  $\text{Ne}^{6+}$  will result in AD dominantly to levels of  $1s^24p$  in  $\text{Ne}^{7+}$ , which cannot effectively increase the populations of  $\text{Ne}^{8+}$ . Note, however, that there are  $1s - np$  ( $n = 7, 8, 9, \dots$ ) resonances from  $\text{Ne}^{5+}$ . The levels belonging to configurations of  $1s2l^3np$  ( $n = 7, 8, 9, \dots$ ) will decay predominantly to levels of  $1s^22lnp$  in  $\text{Ne}^{6+}$ . From these levels of  $\text{Ne}^{6+}$ , there are

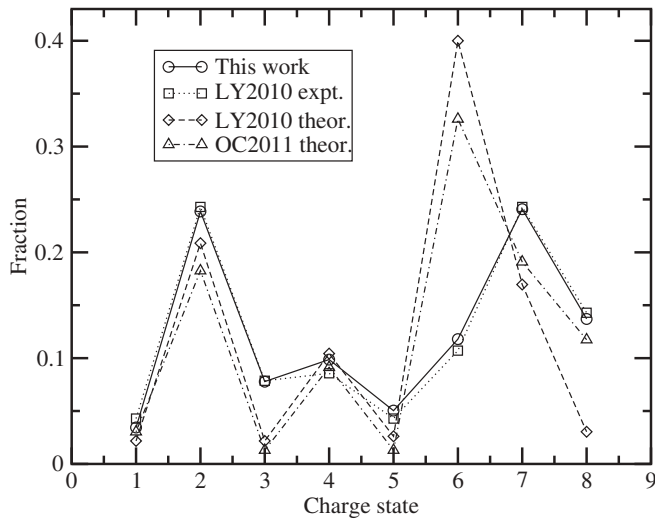


FIG. 3. CSD produced by 1050 eV photon beams. Circles: With all ionization and IRA mechanisms included. Squares: Experiment from Young *et al.* [2]. Diamonds: Theory from Young *et al.* [2]. Triangles: Theory from Ciricosta *et al.* [31].

$1s \rightarrow 3p$  resonance transitions ( $1s^2 2l np - 1s 2l 3 p np$ ) centered near 1050 eV. These core-excited transitions have not been investigated experimentally or theoretically [29,30]. The levels of  $1s 2l 3 p np$  will dominantly decay to  $Ne^{7+}$  via channels of  $1s 2s 2p$  or  $1s 2p^2$ , which will further decay to  $1s^2$  of  $Ne^{8+}$ .

After all PI and IRA mechanisms have been included, the predicted CSD is shown in Fig. 3. The experimental and two other theoretical results obtained by Young *et al.* [2] and by Ciricosta *et al.* [31] are also given in squares, diamonds, and triangles, respectively. With the inclusion of the IRA mechanism, much better agreement with the experiment is found over the whole charge state range from  $Ne^+$  to  $Ne^{8+}$ . Not only is the relative fraction ratio of  $Ne^{6+}$  and  $Ne^{7+}$  reversed,

but also  $Ne^{8+}$  is effectively populated. Moreover, a stronger alternation in the odd-even charge state amplitudes than measured as predicted by Refs. [2,31] is evidently improved in our results.

The IRA effects revealed in this work promise applications in x-ray interactions with atoms, molecules, and clusters. With the increase of atomic number  $Z$ , the electronic structure becomes more and more complicated and, therefore, IRA will become more and more common and should be included. In addition, the pulse duration measurements are experimentally challenging at high photon energies in the x-ray regime [2,32]. Accurate modeling with the IRA effects considered can indirectly help to infer the pulse duration. As the population dynamics is sensitive to the fluence, we can determine the pulse duration if the intensity can be accurately measured, or vice versa.

In conclusion, an inner-shell resonant absorption (IRA) mechanism is proposed to explain the large discrepancy in the charge state distribution of the neon interaction with ultraintense x-ray radiation found between theory and experiment at a photon energy of 1050 eV. The core-excited resonant absorptions from  $1s \rightarrow 4p$  of  $Ne^{6+}$  and  $1s \rightarrow 3p$  of  $Ne^{7+}$  are crucial to the evolution dynamics of the charge state distribution. Their rates are larger than the ionization rates by more than one order of magnitude, and therefore IRA becomes the main absorption mechanism. IRA effects will dominate the evolution dynamics of CSD in x-ray interactions with neon at a wide photon energy range of 850–1350 eV. A complete understanding of the absorption mechanisms including ionization and IRA is pivotal for any further investigations of strong x-ray–matter interactions.

This work was supported by the National Natural Science Foundation of China under Grants No. 11274382 and No. 11274383.

- [1] P. Emma *et al.*, *Nat. Photon.* **4**, 641 (2010).
- [2] L. Young *et al.*, *Nature (London)* **466**, 56 (2010).
- [3] M. Hoener *et al.*, *Phys. Rev. Lett.* **104**, 253002 (2010).
- [4] L. Fang *et al.*, *Phys. Rev. Lett.* **105**, 083005 (2010).
- [5] G. Doumy *et al.*, *Phys. Rev. Lett.* **106**, 083002 (2011).
- [6] H. Thomas *et al.*, *Phys. Rev. Lett.* **108**, 133401 (2012).
- [7] N. Rohringer *et al.*, *Nature (London)* **481**, 488 (2012).
- [8] N. Rohringer and R. Santra, *Phys. Rev. A* **76**, 033416 (2007).
- [9] O. Chuluunbaatar, H. Bachau, Y. V. Popov, B. Piraux, and K. Stefanska, *Phys. Rev. A* **81**, 063424 (2010).
- [10] F. J. Rogers and C. A. Iglesias, *Science* **263**, 50 (1994).
- [11] S. M. Vinko *et al.*, *Nature (London)* **482**, 59 (2012).
- [12] S. X. Hu, B. Militzer, V. N. Goncharov, and S. Skupsky, *Phys. Rev. Lett.* **104**, 235003 (2010).
- [13] J. Bauche, C. Bauche-Arnoult, and M. Klapisch, *Adv. At. Mol. Phys.* **23**, 131 (1987).
- [14] A. Bar-Shalom, J. Oreg, W. H. Goldstein, D. Shvarts, and A. Zigler, *Phys. Rev. A* **40**, 3183 (1989).
- [15] J. Yuan, *Phys. Rev. E* **66**, 047401 (2002).
- [16] J. Zeng, C. Gao, and J. Yuan, *Phys. Rev. E* **82**, 026409 (2010).
- [17] J. Zeng and J. Yuan, *Phys. Rev. E* **76**, 026401 (2007).
- [18] J. Zeng and J. Yuan, *Phys. Rev. E* **74**, 025401(R) (2006).
- [19] S. J. Rose, *High Energy Density Phys.* **5**, 23 (2009).
- [20] C. Gao and J. Zeng, *Phys. Scr. T* **144**, 014037 (2011).
- [21] T. A. Carlson and M. O. Krause, *Phys. Rev. Lett.* **14**, 390 (1965).
- [22] M. O. Krause, M. L. Vestal, W. H. Johnston, and T. A. Carlson, *Phys. Rev.* **133**, A385 (1964).
- [23] T. Schneider, P. L. Chocian, and J. M. Rost, *Phys. Rev. Lett.* **89**, 073002 (2002).
- [24] Y. Hikosaka *et al.*, *Phys. Rev. Lett.* **98**, 183002 (2007).
- [25] D. Mihalas, *Stellar Atmospheres* (Freeman, San Francisco, 1978).
- [26] R. Florido *et al.*, *Phys. Rev. E* **80**, 056402 (2009).
- [27] M. F. Gu, *Astrophys. J.* **582**, 1241 (2003).
- [28] M. F. Gu, *Can. J. Phys.* **86**, 675 (2008).
- [29] A. E. Kramida and M.-C. Buchet-Poulizac, *Eur. Phys. J. D* **39**, 173 (2006).
- [30] A. E. Kramida and M.-C. Buchet-Poulizac, *Eur. Phys. J. D* **38**, 265 (2006).
- [31] O. Ciricosta, H. K. Chung, R. W. Lee, and J. S. Wark, *High Energy Density Phys.* **7**, 111 (2011).
- [32] L. Miaja-Avila *et al.*, *Phys. Rev. Lett.* **97**, 113604 (2006).